Silicon-based optical leaky wave antenna with narrow beam radiation

Qi Song, Salvatore Campione, Ozdal Boyraz, and Filippo Capolino*

Department of Electrical Engineering and Computer Science, University of California, Irvine, California 92617, USA
**f.capolino@uci.edu*

Abstract: We propose a design of a dielectric (silicon nitride) optical leaky wave antenna (OLWA) with periodic semiconductor (silicon) corrugations, capable of producing narrow beam radiation. The optical antenna radiates a narrow beam because a leaky wave (LW) with low attenuation constant is excited at one end of the corrugated dielectric waveguide. We show that pointing angle, beam-width, and operational frequency are all related to the LW complex wavenumber, whose value depends on the amount of silicon perturbations in the waveguide. In this paper, the propagation constant and the attenuation coefficient of the LW in the periodic structure are extracted from full-wave simulations. The far-field radiation patterns in both glass and air environments predicted by LW theory agree well with the ones obtained by full-wave simulations. We achieve a directive radiation pattern in glass environment with about 17.5 dB directivity and 1.05 degree beam-width at the operative free space wavelength of 1.55 μm, pointing at a direction orthogonal to the waveguide (broadside direction). We also show that the use of semiconductor corrugations facilitate electronic tuning of the radiation pattern via carrier injection.

OCIS codes: (230.7390) Waveguides, planar; (050.6624) Sub-wavelength structures.

References and links

1. P. Ghenuche, S. Cherukulappurath, T. H. Taminiau, N. F. van Hulst, and R. Quidant, "Spectroscopic mode mapping of resonant plasmon nanoantennas," Phys. Rev. Lett. **101**(11), 116805 (2008).
2. S. Wedge, J. A. E. Wasey, W. L. Barnes, and I. Sage, "Coupled surface plasmon-polariton mediated photoluminescence from a top-emitting organic light-emitting structure," Appl. Phys. Lett. **85**(2), 182–184 (2004).
3. R. L. Olmon, P. M. Krenz, A. C. Jones, G. D. Boreman, and M. B. Raschke, "Near-field imaging of optical antenna modes in the mid-infrared," Opt. Express **16**(25), 20295–20305 (2008).
4. T. Thio, H. J. Lezec, T. W. Ebbesen, K. M. Pellerin, G. D. Lewen, A. Nahata, and R. A. Linke, "Giant optical transmission of sub-wavelength apertures: physics and applications," Nanotechnology **13**(3), 429–432 (2002).
5. Q. Song, F. Qian, E. K. Tien, I. Tomov, J. Meyer, X. Z. Sang, and O. Boyraz, "Imaging by silicon on insulator waveguides," Appl. Phys. Lett. **94**(23), 231101 (2009).
6. C. K. Toth, "R&D of mobile LIDAR mapping and future trends," in *Proceeding of ASPRS 2009 Annual Conference* (Baltimore, Maryland, 2009).
7. D. R. Jackson, J. Chen, R. Qiang, F. Capolino, and A. A. Oliner, "The role of leaky plasmon waves in the directive beaming of light through a subwavelength aperture," Opt. Express **16**(26), 21271–21281 (2008).
8. A. Micco, V. Galdi, F. Capolino, A. Della Villa, V. Pierro, S. Enoch, and G. Tayeb, "Directive emission from defect-free dodecagonal photonic quasicrystals: a leaky wave characterization," Phys. Rev. B **79**(7), 075110 (2009).
9. E. Colak, H. Caglayan, A. O. Cakmak, A. D. Villa, F. Capolino, and E. Ozbay, "Frequency dependent steering with backward leaky waves via photonic crystal interface layer," Opt. Express **17**(12), 9879–9890 (2009).
10. R. Soref, "The past, present, and future of silicon photonics," IEEE J. Sel. Top. Quantum Electron. **12**(6), 1678–1687 (2006).
11. Q. F. Xu, B. Schmidt, S. Pradhan, and M. Lipson, "Micrometre-scale silicon electro-optic modulator," Nature **435**(7040), 325–327 (2005).
12. L. Friedman, R. A. Soref, and J. P. Lorenzo, "Silicon double-injection electro-optic modulator with junction gate control," J. Appl. Phys. **63**(6), 1831–1839 (1988).

#141139 - $15.00 USD Received 14 Jan 2011; revised 8 Mar 2011; accepted 11 Apr 2011; published 20 Apr 2011

13. C. K. Tang and G. T. Reed, "Highly efficient optical-phase modulator in SOI waveguides," Electron. Lett. **31**(6), 451–452 (1995).
14. K. Van Acoleyen, W. Bogaerts, J. Jágerská, N. Le Thomas, R. Houdré, and R. Baets, "Off-chip beam steering with a one-dimensional optical phased array on silicon-on-insulator," Opt. Lett. **34**(9), 1477–1479 (2009).
15. S. M. Csutak, S. Dakshina-Murthy, and J. C. Campbell, "CMOS-compatible planar silicon waveguide-grating-coupler photodetectors fabricated on silicon-on-insulator (SOI) substrates," IEEE J. Quantum Electron. **38**(5), 477–480 (2002).
16. P. Cheben, S. Janz, D. X. Xu, B. Lamontagne, A. Delage, and S. Tanev, "A broad-band waveguide grating coupler with a subwavelength grating mirror," IEEE Photon. Technol. Lett. **18**(1), 13–15 (2006).
17. A. A. Oliner and D. R. Jackson, "Leaky-wave antennas," in *Antenna Engineering Handbook*, J. Volakis, ed. (McGraw Hill, 2007), pp. 11.11–11.56.
18. F. Capolino, D. R. Jackson, and D. R. Wilton, "Field representation in periodic artificial materials excited by a source," in *Theory and Phenomena of Metamaterials*, F. Capolino, ed. (CRC Press, 2009), p. 12.11.
19. S. Campione and F. Capolino, "Linear and Planar Periodic Arrays of Metallic Nanospheres: Fabrication, Optical Properties and Applications," in *Selected Topics in Metamaterials and Photonic Crystals*, A. Andreone, A. Cusano, A. Cutolo, and V. Galdi, eds. (World Scientific Publishing, 2011).
20. D. R. Jackson and A. A. Oliner, "Leaky-wave antennas," in *Modern Antenna Handbook*, C. A. Balanis, ed. (Wiley, 2008), pp. 325–367.
21. R. E. Collin, *Antennas and Radiowave Propagation* (McGraw Hill, 1985), p. 164.
22. C. A. Balanis, *Antenna Theory: Analysis and Design* (Wiley, 2005), p. 286.
23. E. J. Rothwell and M. J. Cloud, *Electromagnetics* (CRC Press, 2008), p. 418.
24. J. A. Stratton, *Electromagnetic Theory* (McGraw-Hill, 1941), p. 424.
25. K. Preston, S. Manipatruni, A. Gondarenko, C. B. Poitras, and M. Lipson, "Deposited silicon high-speed integrated electro-optic modulator," Opt. Express **17**(7), 5118–5124 (2009).
26. Q. Xu, S. Manipatruni, B. Schmidt, J. Shakya, and M. Lipson, "12.5 Gbit/s carrier-injection-based silicon micro-ring silicon modulators," Opt. Express **15**(2), 430–436 (2007).
27. O. Boyraz, X. Sang, E.-K. Tien, Q. Song, F. Qian, and M. Akdas, "Silicon based optical pulse shaping and characterization," Proc. SPIE **7212**, 72120U (2009).
28. W. P. Dumke, "Minority-carrier injection and storage into a heavily doped emitter—approximate solution for Auger recombination," Solid-State Electron. **24**(2), 155–157 (1981).
29. C. Manolatou and M. Lipson, "All-optical silicon modulators based on carrier injection by two-photon absorption," J. Lightwave Technol. **24**(3), 1433–1439 (2006).

1. Introduction

An optical leaky wave antenna (OLWA) is a device that radiates a light wave into the surrounding space from a leaky wave (LW) guided mode or, vice-versa, it couples receiving optical power from the surrounding space into a guided optical mode. Optical antennas have the capabilities to enhance the interaction between light and matter, and thus have the potential to boost the efficiency of optoelectronic devices such as light-emitting diodes, lasers and solar cells, and bio-chemical detection capabilities [1–3].

The optical antenna cases studied up to date mostly focus on the local field distribution control of the device. Those kinds of antennas are fabricated in a sub-wavelength dimension and some exceptional physical phenomena, such as super-resolution effect and near-field enhancement [4], are realizable due to the resonant modes. Very directive near-IR optical antennas with electronically controlled beam steering and radiation pattern are the subject of great interest for applications such as planar imaging [5] and LIDAR [6]. The dielectric near-IR antenna consisting of silicon perturbations designed here can be used to transform a guided mode into a leaky mode, thus radiating in a region of space. This radiation phenomenon can be precisely described by using the concept of LWs. Accordingly, the periodicity of the silicon perturbations of the waveguide produces a spatial harmonic of the guided mode in the visible region. Recently, LWs parameterization has been used to explain enhanced directivity of a corrugated thin silver film with a sub-wavelength hole [7]. LWs have also been used to parameterize directive radiation from a quasi-crystal waveguide [8], or from a photonic crystal interface layer [9].

In the optoelectronics domain, silicon-on-insulator (SOI) devices have been widely utilized recently to deliver chip scale active and passive photonic devices such as amplifiers, switches and modulators with potential optoelectronic integration on the same platform [10,11]. The SOI platform provides tight mode confinement due to a large index contrast,

#141139 - $15.00 USD Received 14 Jan 2011; revised 8 Mar 2011; accepted 11 Apr 2011; published 20 Apr 2011

which is essential for miniaturization, and simultaneous low loss operation [12]. In particular, the electronic tunability of the optical parameters of silicon (such as refractive index and absorption coefficient) via current injection renders itself the ideal platform for optical antennas that can facilitate electronic beam control [13–15]. The OLWA can function as a passive transmitter or receiver as well as beam steering device. Hence, the integration of a SOI waveguide and an optical antenna is a powerful tool for optical wave guiding and electronically controlled emitters. Previously, directional couplers and sensors devices with periodic perturbations have been presented [14–16]. However, the proposed device in this article includes semiconductor periodic perturbations inside a dielectric waveguide (novel by itself) that facilitate miscellaneous optoelectronic tunability. Also, up to date, far field radiation pattern has not been utilized in the similar sense.

In this paper, we provide results for a novel CMOS compatible OLWA with electronic tuning capability, and most of the investigation is relative to a structure invariant along one direction (say z, Fig. 1). Indeed, though in general waves can also be guided in wide slabs (in the z direction), the results shown provide insight into how a waveguide with rectangular cross section could radiate. The radiation pattern of this latter case, a linear OLWA in a three dimensional (3D) space, is also presented at the end of the paper. The proposed OLWA consists of a silicon nitride (Si_3N_4) waveguide comprising periodic silicon perturbations and it provides directive radiation patterns at communication wavelengths. Modeling of such an antenna indicates that CMOS compatible OLWAs are feasible and produce very directive radiation patterns with about 17.5 dB directivity and 1.05 degree beam-width pointing at a direction orthogonal to the waveguide direction (transverse radiation, also called broadside radiation). We show that the use of semiconductor corrugations facilitates electronic tuning of the radiation pattern via carrier injection. The Floquet theorem is adopted here to describe the periodic properties of the field inside the waveguide and LW theory is provided to give the physical explanation for the narrow beam radiation behavior. The propagation constant and the attenuation coefficient of the leaky wave propagating in the periodic structure are extracted from full-wave simulations and utilized to evaluate the far-field radiation patterns in both SiO_2 and air environments by using the theoretical formulas provided. Results demonstrate that the theoretical predictions are in excellent agreement with radiation patterns obtained by full-wave simulations.

The structure of the paper is as follows. The geometry of the proposed antenna is presented in Sec. 2. In Sec. 3, we summarize the underlying leaky wave radiation phenomenon of the single-mode waveguide including the periodic perturbations. Enhanced directivity has been related to leaky wave excitation. Based on that, we estimate the radiation pattern adopting two different approaches: i) the equivalent aperture field method and ii) the array factor method. The physical explanation for the narrow beam radiation at broadside is given in detail. The theoretical analyses are compared with full-wave simulation results obtained by using two different commercial software packages, COMSOL and HFSS, in Sec. 4. Also, the far-field radiation patterns have been obtained from full-wave simulations by computing the far-field from the near-field in both SiO_2 and free space environments, as well as directly computed by the software in air in the same section to verify the radiation pattern in the far-field. In Sec. 5 we provide a discussion on carrier injection to assess the electronic tunability of the radiation pattern. Finally, in Sec. 6, we discuss a possible 3D implementation for the proposed OLWA.

2. Antenna geometry

The two dimensional (2D) structure of the OLWA is presented in Fig. 1, assumed invariant along the z direction. The optical guided mode is excited from the left side. The same mode is used to feed the OLWA made of 60 periodic silicon perturbations positioned on the bottom side of the silicon nitride waveguide. This number has been observed to be large enough to provide a long radiating section, with length L, required to achieve high directivity. The

#141139 - $15.00 USD Received 14 Jan 2011; revised 8 Mar 2011; accepted 11 Apr 2011; published 20 Apr 2011

physical dimensions of the silicon perturbation are parametrically studied to obtain high directivity around the bottom transverse direction (radiation along $-y$ in Fig. 1). Power radiation takes place towards $\pm y$ directions. However, the radiation is stronger in the bottom transverse direction due to the fact that the perturbation is placed on the bottom side of the waveguide. Each silicon perturbation is characterized by a width and a length equal to $w = 300$ nm and $l = d/2 = 485$ nm, respectively, where $d = 970$ nm is the period of the perturbation. The waveguide is placed on a silica glass (SiO_2) substrate and is covered by a SiO_2 cover layer, and has a width $t_w = 1$ μm. The total length of the radiating section is $L = Nd$, where N is the number of the perturbation, chosen equal to 60 in this study.

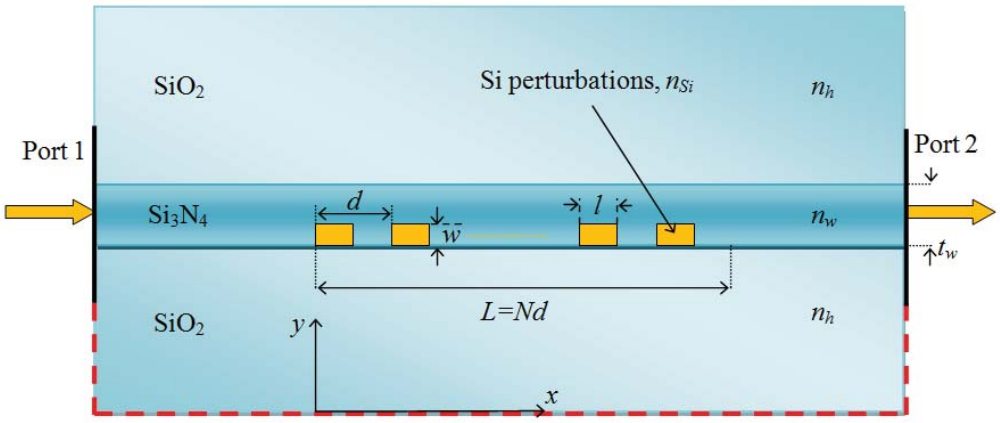

Fig. 1. Optical antenna based on SOI. The Si periodic perturbation ($n_{Si} = 3.48$) is inside the Si_3N_4 waveguide ($n_w = 1.67$). The waveguide has a width equal to $t_w = 1$ μm, is upon a SiO_2 substrate ($n_h = 1.45$) and is covered by a SiO_2 layer. The Si perturbation is characterized by an optimized period $d = 970$ nm, a width $w = 300$ nm and a length $l = d/2 = 485$ nm, which are found after a parametric study. The number of elements of the perturbation is equal to 60. The red contour represents the boundary at which the field has been extracted for far-field calculations.

3. Local field representations and far-field pattern theoretical derivations

In this section, Floquet theory specialized in one dimensional domain is introduced as a powerful tool to characterize the behavior of a SOI waveguide comprising a periodic perturbation. The equivalent aperture (EA) method and the array factor (AF) method are the two theoretical approaches proposed to predict far-field radiation patterns from a leaky wave produced by the presence of the silicon perturbation inside the waveguide. In this analysis, electromagnetic fields are assumed to be time harmonic with a $\exp(-i\omega t)$ time variation.

3.1 Quasi-periodic field distribution along the periodic structure

The guided mode excited by the incoming field on the left side of the waveguide becomes leaky in correspondence of the periodic silicon perturbations. Such a mode decays exponentially along the structure, even for a lossless structure, and a leakage phenomenon (radiation) takes place.

In the 2D structure presented here, the electric field is polarized along z and travels along the x direction. Indeed, the problem is invariant in the z-direction and the z-component of the guided electric field satisfies the quasi-periodic property $E(x+d,y) = E(x,y)\exp(ik_{x,0}d)$, where d is the period of the periodic structure and $k_{x,0} = \beta + i\alpha$ is the wavenumber along the

#141139 - $15.00 USD Received 14 Jan 2011; revised 8 Mar 2011; accepted 11 Apr 2011; published 20 Apr 2011

propagation direction. Here, β and α are the phase and attenuation constants, respectively, of the LW. Note that, before introducing the perturbations, the original guided mode has a phase propagation constant very close to β, whereas the attenuation constant of the waveguide would be much smaller than α (without perturbation the attenuation is caused only by material losses and scattering by irregularities of the structure). Instead, with perturbations, the value of α can be significantly large because of radiation, though to have a directive OLWA this value has to be maintained low. Accordingly, in terms of a Fourier series expansion, the electric field at any place along the periodic structure can be represented as the superposition of Floquet spatial harmonics

$$E(x,y)=\sum_{n=-\infty}^{\infty}E_n(y)e^{ik_{x,n}x},\quad k_{x,n}=k_{x,0}+2n\pi/d, \tag{1}$$

where $k_{x,n}$ is the Floquet wavenumber, n is the order of the Floquet spatial harmonic, and $E_n(y)$ is the weight of the n-th harmonic [17–19]. Each Floquet wave number $k_{x,n}=\beta_n+i\alpha$ has the same attenuation constant α [7,20]. The purpose of the periodic perturbations is to create a radiating $n=-1$ harmonic. Its wavenumber is

$$k_{x,-1}=\beta_{-1}+i\alpha,\ \text{with}\ \beta_{-1}=\beta-2\pi/d, \tag{2}$$

such that $-k_h<\beta_{-1}<k_h$, where $k_h=n_hk_0$, k_0 is the free space wavenumber, and n_h is the refractive index of the surrounding material, that in our case is either SiO_2 ($n_h=1.45$) or free space ($n_h=1$).

Therefore, in the periodic structure under analysis, all the n-indexed Floquet harmonics but one are evanescent waves (contrarily to what may happen in gratings where several harmonics have β_n in the visible region, i.e., the wavenumber region $-k_h<\beta_n<k_h$ relative to waves that can propagate away from the plane). The radiating harmonic, the one that falls in the interval $(-k_h,k_h)$, is usually defined as the $n=-1$ one since in slightly perturbed structures the 0th fundamental propagation constant $\beta\equiv\beta_0>k_h$ has a value very close to the one of the bound mode in the unperturbed waveguide, and thus it is not radiating.

3.2 The equivalent aperture method

Based on the Floquet field expansion [Eq. (1)], the electric field along the periodic structure can be described as a superposition of field terms, and only the $n=-1$ is relevant for radiation. Therefore, its expression evaluated on the "aperture" (i.e, a section from where we assume radiation is propagating away [21]) is

$$E(x)=E_{-1}e^{i\beta_{-1}x}e^{-\alpha x}\qquad(0<x<L), \tag{3}$$

where L is the total length of the silicon perturbation, and E_{-1} is the amplitude of the $n=-1$ harmonic of the electric field at the beginning of the silicon perturbation.

The beam radiation angle is related to the $n=-1$ spatial harmonic propagation constant in Eq. (2) by the expression $\beta_{-1}=k_h\cos\phi$; therefore, radiation at broadside (i.e., direction orthogonal to the waveguide, at angle $\phi=\pm\pi/2$) is then obtained when $\beta_{-1}<<k_h$.

The far-field radiation pattern $E^{FF}(\phi)$ is obtained by integrating Eq. (3) across an "equivalent aperture" $(0<x<L)$

#141139 - $15.00 USD Received 14 Jan 2011; revised 8 Mar 2011; accepted 11 Apr 2011; published 20 Apr 2011

$$E^{FF}(\phi) = E_{-1}\int_0^L e^{i\beta_{-1}x}e^{-\alpha x}e^{-ik_h\cos\phi x}dx = E_{-1}\frac{e^{-i(k_h\cos\phi-\beta_{-1}-i\alpha)L}-1}{-i(k_h\cos\phi-\beta_{-1}-i\alpha)} \tag{4}$$

which leads to a normalized far-field pattern magnitude

$$F(\phi) = \frac{\left|E^{FF}(\phi)\right|}{\left|E_{-1}\right|} = \left(\frac{1+e^{-2\alpha L}-2e^{-\alpha L}\cos\left[\left(k_h\cos\phi-\beta_{-1}\right)L\right]}{\left(k_h\cos\phi-\beta_{-1}\right)^2+\alpha^2}\right)^{\frac{1}{2}}, \tag{5}$$

that in the case of large αL (either when the antenna is long, or when the attenuation constant is large) can be further simplified.

The maximum radiation direction can be computed using Eq. (5). In the case of large αL (i.e. when $\exp(-\alpha L) << 1$), the maximum value of $F(\phi_{\max}) = 1/\alpha$ occurs at $\phi = \phi_{\max}$ such that $\cos\phi_{\max} = \beta_{-1}/k_h$. In a similar way, using Eq. (5), it is also possible to determine the 3 dB beam-width, defined as $\Delta\phi_{3\text{dB}} = \left|\phi^+_{3\text{dB}} - \phi^-_{3\text{dB}}\right|$, where $F(\phi^{\pm}_{3\text{dB}}) = F(\phi_{\max})/\sqrt{2}$, which happens when $\cos\phi^{\pm}_{3\text{dB}} \approx (\beta_{-1} \pm \alpha)/k_h$. This leads to

$$\Delta\phi_{3\text{dB}} \approx \frac{2\alpha}{k_h} \tag{6}$$

3.3 The array factor method

The periodic perturbation in the waveguide can be considered as an array of identical scatterers from which the far-field pattern is determined by the pattern multiplication, i.e., by multiplying the pattern of the single element and the array factor (AF) of the array [22]. The pattern of the single perturbation element is quasi isotropic, whereas the array factor is very angle-selective. Therefore, as usual for directive antennas, the total far-field radiation pattern is approximated as $E^{FF}(\phi) \propto AF(\phi)$, and thus $AF(\varphi)$ represents the normalized far-field. For the OLWA under consideration, the array factor $AF(\phi)$ is defined as

$$AF(\phi) = \sum_{n=0}^{N-1} e^{i(\beta_{-1}+i\alpha)nd}e^{-i(k_h\cos\phi)nd} = \frac{1-e^{-i(k_h\cos\phi-\beta_{-1}-i\alpha)Nd}}{1-e^{-i(k_h\cos\phi-\beta_{-1}-i\alpha)d}}, \tag{7}$$

whose magnitude is

$$\left|AF(\phi)\right| = \left(\frac{1+e^{-2\alpha L}-2e^{-\alpha L}\cos\left[\left(k_h\cos\phi-\beta_{-1}\right)L\right]}{1+e^{-2\alpha d}-2e^{-\alpha d}\cos\left[\left(k_h\cos\phi-\beta_{-1}\right)d\right]}\right)^{\frac{1}{2}}, \tag{8}$$

where we have assumed that $L = Nd$. An analogous procedure was applied in [7] to find the directive radiation pattern of a narrow slit in a corrugated silver film.

4. Analysis of the radiation properties

In this section, in order to validate the theoretical results, full-wave simulations are implemented by using two commercial software, COMSOL and HFSS. Explanations of particular phenomena will be provided.

The input light used in these analyses is characterized by a free space wavelength equal to $\lambda_0 = 1.55$ μm, and is polarized along *z*. The actual simulated structure presents a calculation

#141139 - $15.00 USD Received 14 Jan 2011; revised 8 Mar 2011; accepted 11 Apr 2011; published 20 Apr 2011

domain in the *x*-*y* plane of 200 μm × 40 μm. Therefore, there are two waveports, 200 μm apart, one as input (marked as Port 1 in Fig. 1) whereas the other one (marked as Port 2 in Fig. 1) is used to monitor the power remaining after the OLWA section. The width of the SiO_2 layers is 19.5 μm, above and below.

4.1 Preliminary analyses

Figure 2 shows the comparison of the *S*-parameters obtained by COMSOL and HFSS, which are in agreement in all the analyzed wavelength range. It can be observed that S_{11} is lower than −10 dB at $\lambda_0 = 1.55$ μm and almost in the entire swept range. Therefore, just a very small portion of the power injected to the antenna will be reflected back by the silicon perturbations. In other words, the power accepted by the antenna will be close in value to the incident power furnished by the incoming wavemode at the input. The transmission coefficient S_{21} is smaller than −20 dB at $\lambda_0 = 1.55$ μm and in almost all the analyzed range. Therefore, very small percentage of power travelling along the waveguide will pass the silicon perturbation section. All the incident power is either lost by dissipation (material losses) or by radiation. Since material losses are much smaller than radiation losses, as stated in Sec. 3.1, we can consider that all the power has been radiated away. Note that there is a mismatch between COMSOL and HFSS only below −35 dB mostly due to different numerical precisions of the two software packages.

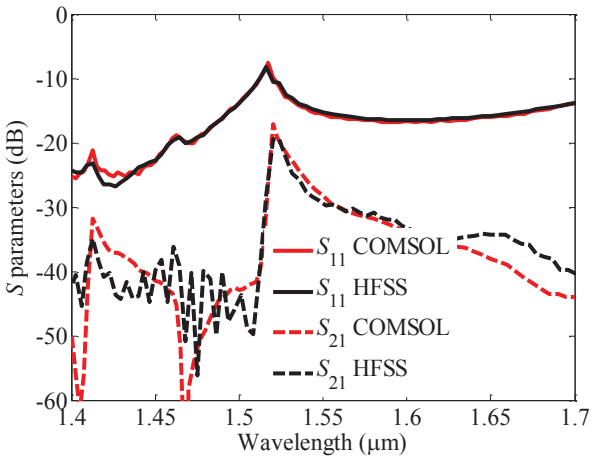

Fig. 2. Comparison of the *S*-parameters obtained by COMSOL and HFSS with respect to the free space wavelength λ_0 varying from 1.4 μm to 1.7 μm.

4.2 Local field across the aperture

Having assured that the proposed structure radiates, we then proceed on the analysis by computing the parameters characterizing the LW from the results obtained by full-wave simulations.

From Eq. (3), it is clear that the description of the aperture field is described by means of two parameters: the propagation constant β_{-1} and the attenuation constant α. After having computed these parameters, the far-field radiation pattern can be easily constructed using the two theoretical methods presented in Sec. 3. The field along the silicon-perturbed waveguide contains the information regarding the two parameters stated above. Indeed, we know that the local field magnitude decays exponentially along the perturbed waveguide with attenuation

#141139 - $15.00 USD Received 14 Jan 2011; revised 8 Mar 2011; accepted 11 Apr 2011; published 20 Apr 2011

constant α. Moreover, its phase shift is linearly dependent to the propagation constant, as can be seen looking at the phase term $\beta_{-1}x$.

Figures 3(a) and 3(b) show the field magnitude and phase along the silicon-perturbed waveguide, sampled at one point per cell, positioned at the center of each Si perturbation, along *x,* and at the bottom of each Si perturbation, along *y*. The magnitude of the field $E(x)$ in Fig. 3(a) exhibits a linear trend using a logarithmic scale, confirming its exponential decay along the waveguide longitudinal direction as expected from $\left|E(x)/E_{-1}\right|_{\mathrm{dB}} = 20\log e^{-\alpha x} = -20\alpha x \log e$. As can be easily inferred, the attenuation constant α can be measured from the slope of the line in Fig. 3(a). Figure 3(b) shows, instead, the unwrapped phase $\beta_{-1}x$ of the leaky wave along the waveguide: the slope of the line provides the propagation constant β_{-1}. Observing one sample of the field per period gives us only the phase propagation constant in the main Brillouin zone.

We used the least mean square interpolation to extract the above mentioned LW parameters. The wavenumber is equal to $\beta_{-1} = -2.46\times10^{5}\,\mathrm{m}^{-1}$. The normalized propagation constant with respect to the free space wavenumber is $\bar{\beta}_{-1} = \beta_{-1}/k_0 \approx -0.06$. In the same way, the extracted value of the attenuation constant is $\alpha = 4.52\times10^{4}\,\mathrm{m}^{-1}$, which corresponds to the normalized value $\bar{\alpha} = \alpha/k_0 \approx 0.01$.

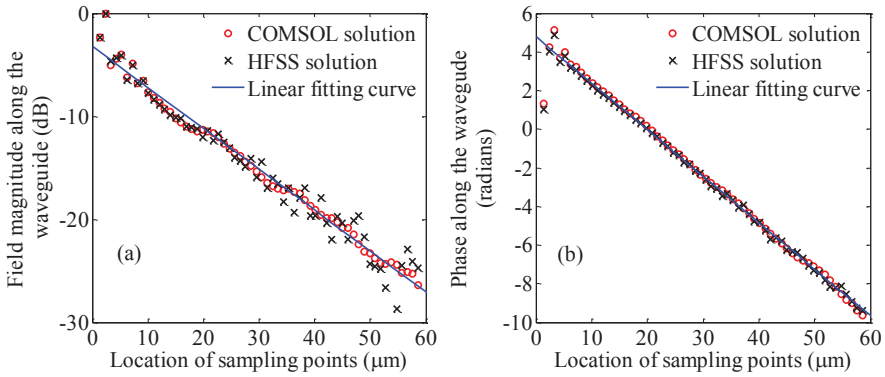

Fig. 3. Comparison between COMSOL and HFSS full-wave simulation results for the electric field along the waveguide, sampled in the silicon perturbations (one point per cell). (a) The magnitude and (b) the phase of the electric field along the aperture.

4.3 Far-field radiation pattern in free space and SiO_2 environments

As we have demonstrated in Sec. 3, the far-field radiation pattern can be obtained theoretically by applying two different approaches: the equivalent aperture method, leading to Eq. (5), and the array factor method, leading to Eq. (8). The far-field radiation patterns are then analytically computed by using the previously extracted values for α and β_{-1} into Eq. (5) and Eq. (8) for both free space and SiO_2 environments.

Far-field radiation patterns in environments different from free space cannot be obtained by COMSOL and HFSS; for this reason, the Stratton-Chu integral equation [23,24] is used to numerically implement the far-field radiation pattern transformation via the extracted fields along the red contour in Fig. 1, at the boundary between SiO_2 and free space. The transformation between near- and far-field will be here referred to as near-field integration. We compared then our near-field integration assuming free space outside the SiO_2 geometry in Fig. 1, with the patterns directly provided by COMSOL and HFSS, and observed perfect

#141139 - $15.00 USD Received 14 Jan 2011; revised 8 Mar 2011; accepted 11 Apr 2011; published 20 Apr 2011

agreement. For this reason, we show next just the patterns derived from the near-field integration of the data provided by COMSOL and HFSS.

The free space far-field radiation patterns, assuming free space outside the SiO_2 region, are shown in Fig. 4. The red and black lines are the results obtained by near-field integration of fields obtained by COMSOL and HFSS, respectively. Whereas the green and blue lines are the EA method and the AF method results, respectively, considering 60 silicon perturbations.

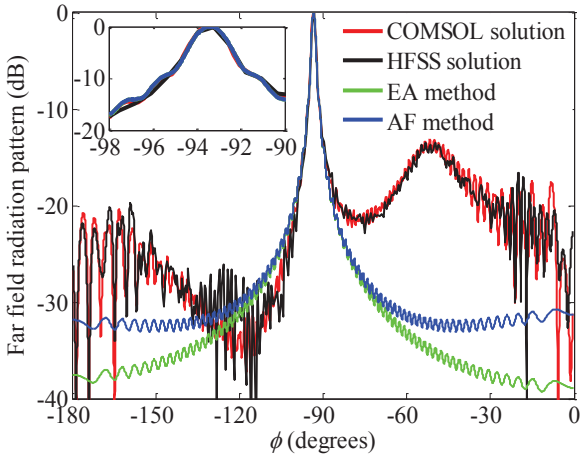

Fig. 4. Comparison of the normalized far-field radiation patterns in free space, obtained by COMSOL (red line), HFSS (black line), EA method (green line) and AF method (blue line). The inset shows an enlargement of the maximum radiation region.

The far-field radiation patterns of the main directive beam obtained with the LW theory are in good agreement with the full-wave simulation results, down to –20 dB. The full-wave simulation results present a very directive main-beam around $-93.2°$. This peak position is in agreement with the approximate value computed in Sec. 3.2, $\phi_{\max} \approx \arccos(\beta_{-1}/k_h) = -93.5°$. We have computed the directivity by

$$D = \frac{2\pi \left| E_{\max}^{FF} \right|^2}{\int_0^{2\pi} \left| E^{FF}(\phi) \right|^2 d\phi}, \tag{9}$$

Where $E_{\max}^{FF}$ represents the electric far-field along the direction $\phi_{\max}$ of maximum radiation obtained by either HFSS or COMSOL. This leads to 15.7 dB directivity. The full-wave simulation 3 dB beam-width is $\Delta\phi_{3\text{dB}} \approx 1.4°$, in agreement with the approximate formula (6) which gives $\Delta\phi_{3\text{dB}} \approx 1.3°$.

The side-lobe at around $-51°$ in Fig. 4 is not predicted by LW theory based on the values α and β_{-1} found in Sec. 4.2. Indeed, a different phase behavior is observed in Fig. 3 for a few elements at the beginning of the silicon perturbations. The side-lobe is explained by noticing that the first two/three elements of the perturbation form a small array. Indeed, if we interpolate the first two (three) points in Fig. 3(b), we are able to extract the value $\beta_{-1} = 3.02\times10^6\,\text{m}^{-1}$ ($\beta_{-1} = 1.95\times10^6\,\text{m}^{-1}$). According to the array factor for these two sub-arrays made of 2 (3) elements, respectively, the maximum radiation ϕ_M is obtained when $k_h \cos\phi_M - \beta_{-1} = 0$, as inferred from Eq. (8). These two different β_{-1} values result in a

#141139 - $15.00 USD Received 14 Jan 2011; revised 8 Mar 2011; accepted 11 Apr 2011; published 20 Apr 2011

maximum at $\phi_M \approx -42°$ ($\phi_M \approx -61°$), which are close to the one obtained by full-wave simulations at around $\phi \approx -51°$, observed in Fig. 4.

Figure 5 shows COMSOL results of the far-field radiation pattern around the main beam, assuming free space outside the SiO_2 region, when operating at different free space wavelengths. The maximum radiation angle has a clockwise shift from $-88.8°$ to $-94°$ with 70 nm wavelength increase from $\lambda_0 = 1.49$ μm to $\lambda_0 = 1.56$ μm. The 3 dB beam-width becomes narrower from $\Delta\phi_{3\text{dB}} \approx 2.7°$ to $\Delta\phi_{3\text{dB}} \approx 1.4°$.

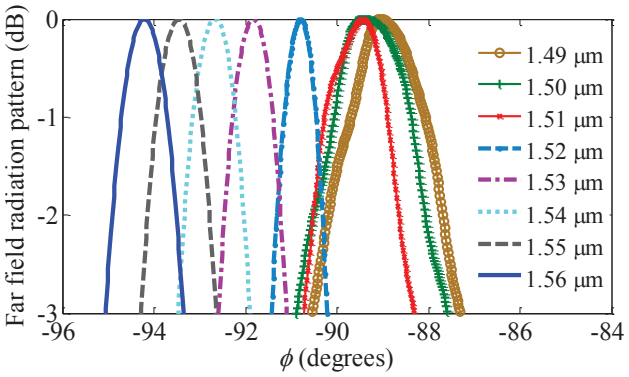

Fig. 5. COMSOL results of the normalized far-field radiation pattern in free space by varying the free space wavelength λ_0 varying from 1.49 μm to1.56 μm.

Figure 6 shows the far-field patterns assuming that the SiO_2 region extends beyond the dashed red line shown in Fig. 1. The red and black lines are the results obtained by COMSOL and HFSS, respectively. Whereas the green and blue lines are the EA method and the AF method results, respectively, considering 60 silicon perturbations. The full-wave simulation results present a very directive main-lobe at $-92.5°$. Again, this peak position is in agreement with the approximate value that, adopting the formula provided in Sec. 3.2, is $\phi_{\max} \approx \arccos(\beta_{-1}/k_h) = -92.4°$.

The side-lobe at $-65°$ in Fig. 6 is not predicted by LW theory based on the values α and β found in Sec. 4.2. The same approach adopted in the case of free space environment can be used here to explain the side-lobe in Fig. 6, estimating the maximum radiation of the sub-array of 2 or 3 elements radiating at $\phi_M \approx -60°$ or $\phi_M \approx -71.3°$, respectively, close to the observed one at $-65°$.

The directive radiation has been obtained by either HFSS or COMSOL, resulting into 17.5 dB directivity by using Eq. (9). The full-wave simulation 3 dB beam-width is $\Delta\phi_{3\text{dB}} \approx 1.05°$, in agreement with the approximate formula (6) which gives $\Delta\phi_{3\text{dB}} \approx 0.9°$.

Figure 7 illustrates the COMSOL results of the far-field radiation pattern when operating at different free space wavelengths of the incoming wave mode. It is noted that as far as the wavelength increases (frequency decreases), the maximum radiation angle turns in a clockwise way. In particular, with 70 nm wavelength increase from $\lambda_0 = 1.49$ μm to $\lambda_0 = 1.56$ μm, the radiation peak has shifted from $-88.8°$ to $-92.9°$. It can be observed that not only the peak moves by varying the wavelength, but also the 3 dB beam-width becomes narrower, from $\Delta\phi_{3\text{dB}} \approx 2.2°$ to $\Delta\phi_{3\text{dB}} \approx 1°$.

#141139 - $15.00 USD Received 14 Jan 2011; revised 8 Mar 2011; accepted 11 Apr 2011; published 20 Apr 2011

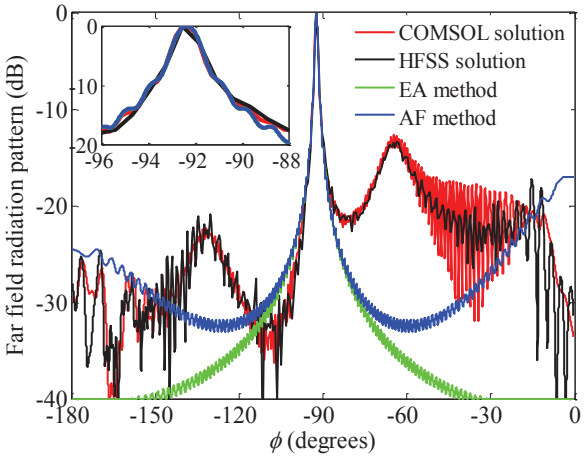

Fig. 6. Comparison of the normalized far-field radiation patterns in SiO_2, obtained by COMSOL (red line), HFSS (black line), EA method (green line) and AF method (blue line). The inset shows an enlargement of the maximum radiation region.

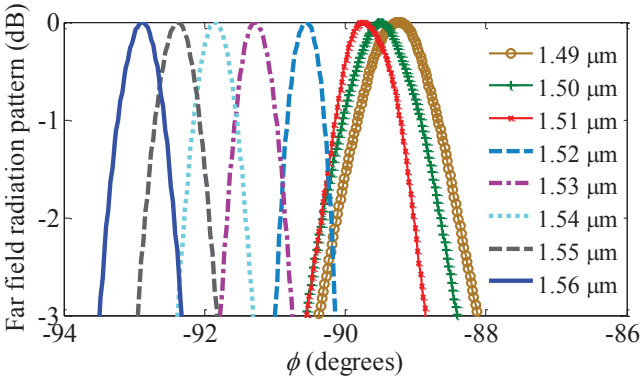

Fig. 7. COMSOL results of the normalized far-field radiation pattern in SiO_2, by varying the free space wavelength λ_0 from 1.49 μm to1.56 μm.

To conclude the analysis on the radiation pattern of the OLWA, we mention that power is also radiated in the region $0° < \phi < 180°$, Fig. 1, with a maximum at $\phi = 93.2°$ in free space and at $\phi = 92.5°$ in silica glass, though radiation toward the bottom side of the waveguide is stronger. The correspondent far-field maxima in the top side of the waveguide are 2.5 dB (free space environment) or 5 dB (silica glass environment) lower than the maxima in the correspondent bottom side direction. Radiation in the region $0° < \phi < 180°$ can be avoided by adding reflectors.

5. Modulation by carrier injection

Linear and non-linear optical properties of silicon have attracted many researchers to develop chip scale planar optical devices on the same optoelectronic platform that is compatible with high density electronic integration [25]. In particular, integration of electronic control to manipulate the optical properties of silicon led to development of novel switches and modulators that can provide solution for telecom applications. The plasma dispersion effect is one of effective phenomena to realize high-speed modulation in silicon waveguides [26]. The basic tuning parameter in these devices is the carrier density that can alter both the Si

#141139 - $15.00 USD Received 14 Jan 2011; revised 8 Mar 2011; accepted 11 Apr 2011; published 20 Apr 2011

refractive index (unitless) and the attenuation coefficient (m^{-1}) as described by the Drude's model [27]

$$\Delta n_{Si}\left(N_e, N_h\right) = -\left(8.8\times10^{-4} N_e + 8.5 N_h^{0.8}\right)\times10^{-18}, \tag{10}$$

$$\Delta\alpha_{Si}\left(N_e, N_h\right) = \left(8.5 N_e + 6.0 N_h\right)\times10^{-16}, \tag{11}$$

where N_e and N_h are the concentrations of electrons and holes (expressed in cm^{-3}) in Si, and k_0 is the free space wavenumber (expressed in m^{-1}). Practically, the density of electrons and holes in Si can be increased up to $10^{19}\,\mathrm{cm}^{-3}$ in optoelectronic devices via current injection or photo generation before Auger process starts to mitigate the device performance [28]. Hence the variation in both the refractive index and the attenuation coefficient due to carrier injection may be significant to facilitate the electronic control of the radiation pattern of OLWAs.

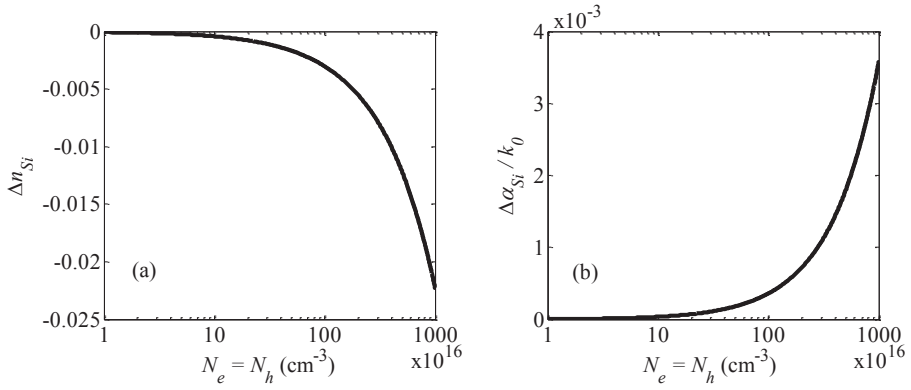

Fig. 8. The variation of (a) the silicon refractive index and (b) the normalized attenuation constant in silicon versus the injected carrier density. The carrier density $N_h = N_e$ varies from $10^{16}\mathrm{cm}^{-3}$ to $10^{19}\ \mathrm{cm}^{-3}$.

To assess the true variations in the radiation pattern in presence of carrier injection into silicon perturbations, we may assume a simple model where we have equal concentration of holes and electrons, or $N_h = N_e$. The presence of $N_h = N_e = 10^{19}\,\mathrm{cm}^{-3}$ free carriers reduces the refractive index of silicon, Δn_{Si}, by 0.0223, as illustrated in Fig. 8(a), whereas it increases the normalized attenuation constant, $\Delta\bar{\alpha}_{Si} = \Delta\alpha_{Si}/k_0$, by 3.6×10^{-3} as shown in Fig. 8(b).

From previous analyses, we know that the radiation pattern at the transverse direction highly depends on the attenuation coefficient of the antenna and the effective index. By using the previous analysis shown in Fig. 8, we can estimate the tunability of the radiation pattern for various carrier injection rates. For instance, the normalized far-field pattern magnitude $F(\phi)$ at peak radiation angle, $\phi = \phi_{\max}$, can be estimated in SiO_2 environment by using (5). In a first order approximation, the modified propagation constant in presence of carrier injection can be expressed as $\beta'_{-1} = \beta_{-1} + ff\,\Delta n_{Si} k_0$, where ff is the filling factor of silicon perturbations (i.e., the percentage of Si volume per unit cell of the OLWA); whereas the attenuation constant in presence of carrier injection can be expressed as $\alpha' = \alpha + ff\,\Delta\bar{\alpha}_{Si} k_0$.

#141139 - $15.00 USD Received 14 Jan 2011; revised 8 Mar 2011; accepted 11 Apr 2011; published 20 Apr 2011

Thus, expressing the electric far-field magnitude ratio between the field at $\phi = \phi_{\max}$ in presence and in absence of carrier injection, we obtain the following equation

$$Q = \frac{F\left(\phi_{\max}, \Delta n_{si}\right)}{F\left(\phi_{\max}, 0\right)} = \frac{\alpha}{1 - e^{-\alpha L}} \left(\frac{1 + e^{-2\alpha' L} - 2e^{-\alpha' L} \cos\left[-\left(ff\, \Delta n_{Si} k_0\right) L\right]}{\left(ff\, \Delta n_{Si} k_0\right)^2 + \alpha'^2} \right)^{\frac{1}{2}}, \quad (12)$$

where $F\left(\phi_{\max}, \Delta n_{si}\right)$ and $F\left(\phi_{\max}, 0\right)$ are the far-field magnitude at maximum radiation angle in presence and in absence of carrier injection, respectively, given in Eq. (5).

In Sec. 4.2 we have extracted $\beta_{-1} = -2.46 \times 10^5\ \mathrm{m}^{-1}$, whereas the attenuation constant α will be considered here as a varying parameter. Also, as stated at the beginning of this paper, the period of the silicon perturbations is $d = 970$ nm and the width of each perturbation is $w = 300$ nm, thus the filling factor is $ff = 15\%$. The total length of the perturbed waveguide is $L = Nd = 58.2\ \mu$m, with $N = 60$.

In Fig. 9 we show the variation of Q in Eq. (12) for some examples of different values of the LW attenuation constant (before carrier injection) equal to $\alpha = 0.01 k_0$, $\alpha = 0.005 k_0$ and $\alpha = 0.001 k_0$. Figure 9 indicates that $Q \approx -0.52$ dB at the carrier injection of $N_h = N_e = 10^{19}\ \mathrm{cm}^{-3}$ when $\alpha = 0.01 k_0$. The value changes to $Q \approx -0.65$ dB and $Q \approx -0.75$ dB when $\alpha = 0.005 k_0$ and $\alpha = 0.001 k_0$, respectively.

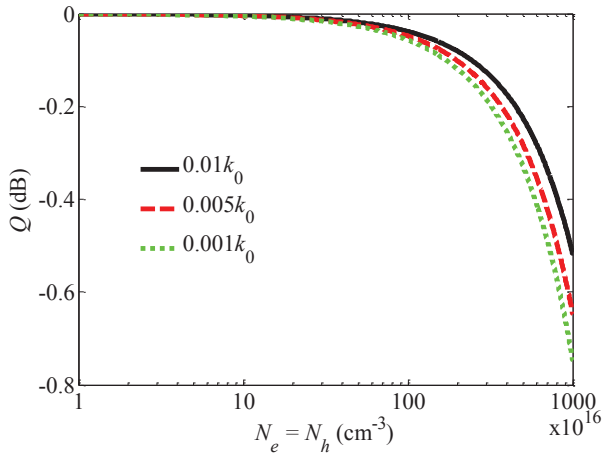

Fig. 9. The variation of Q at broadside versus the injected carrier density. The carrier density $N_h = N_e$ varies from $10^{16}\ \mathrm{cm}^{-3}$ to $10^{19}\ \mathrm{cm}^{-3}$.

The preliminary results presented in Fig. 9 indicate that the effect of carrier injection on the power radiated at a certain direction is rather limited (–0.52 dB with a LW attenuation constant $\alpha = 0.01 k_0$ which is similar to the one extracted by full-wave simulations in Sec. 4.2). One way of amplifying weak perturbations in the optical domain is achieved by placing perturbations into optical resonators so that these perturbations will be experienced by the optical field during multiple roundtrips [29]. Indeed, it has been already demonstrated theoretically and experimentally that weak perturbations created via injection of carriers into silicon optical resonators alter the resonance wavelength and the quality factor of the resonator and provide modulation of the optical signals [29]. Similarly, by integrating OLWAs into a racetrack or Fabry-Perot integrated cavities, it is expected to amplify the

#141139 - $15.00 USD Received 14 Jan 2011; revised 8 Mar 2011; accepted 11 Apr 2011; published 20 Apr 2011

–0.52 dB perturbation in the radiation pattern of an amount which is proportional to the quality factor of the cavity. Future research should be dedicated to quantify the perturbations in the radiation pattern in resonators with practical geometries.

6. Three dimensional design of a linear OLWA

In the previous sections we have analyzed the 2D model (i.e, a structure invariant along the z direction) of the proposed OLWA. Though the 2D model is by itself of practical interest as slab waveguide with periodic perturbations, it is important to show how our proposed OLWA can be implemented in 3D. Radiation from a linear OLWA will exhibit high directivity in the xy plane. The design steps and the working principle are the same as those highlighted in Sec. 2: radiation is caused by a low-attenuation leaky mode with −1 harmonic having a very small wavenumber.

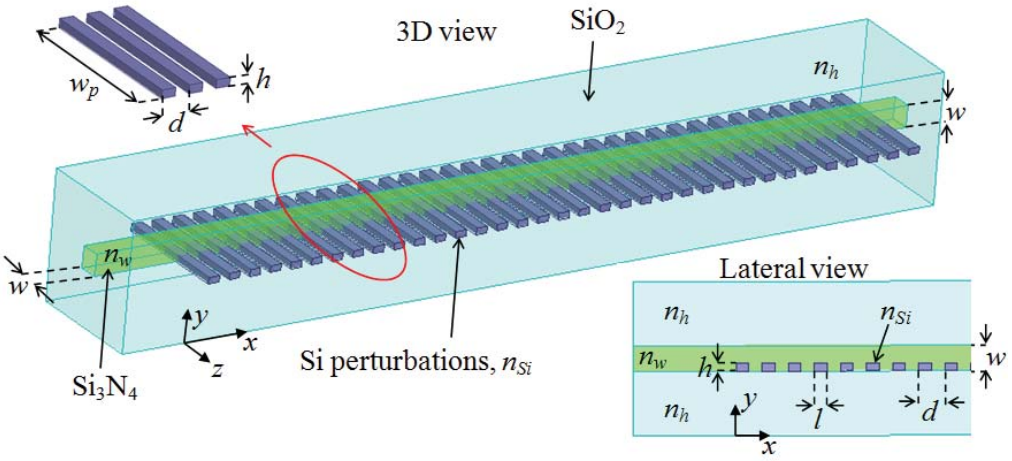

Fig. 10. 3D model for a linear OLWA. Notice that the lateral view is as in the 2D model.

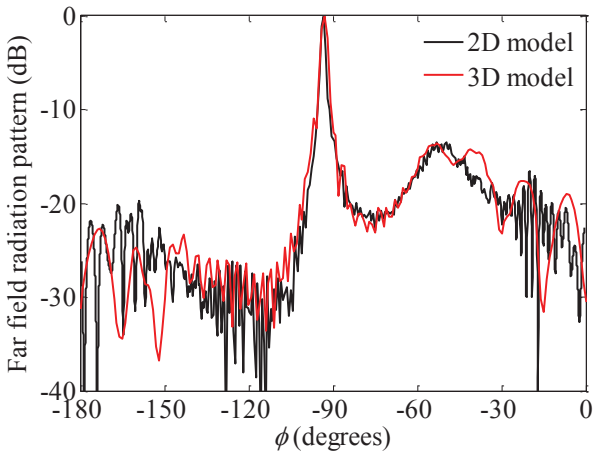

Fig. 11. Comparison of the far-field radiation patterns in the xy plane of 2D and 3D optical leaky wave antennas. In both cases a narrow radiating beam is obtained.

The 3D geometry reported in Fig. 10 consists of the Si_3N_4 waveguide with square cross section $w \times w$, with $w = 1\ \mu m$ and $39.285\ \mu m$ long. It is embedded in a SiO_2 volume with cross section equal to $6\ \mu m \times 6\ \mu m$. The number N of perturbations is now chosen equal to 35

#141139 - $15.00 USD Received 14 Jan 2011; revised 8 Mar 2011; accepted 11 Apr 2011; published 20 Apr 2011

(because of the high numerical simulation burden of 3D structures), and each perturbation extends to the edge of the silica glass domain (characteristic that will be adopted to perform carrier injection in future works, as discussed in Sec. 5). Each silicon perturbation has the following dimensions: $w_p = 6$ μm, $h = 300$ nm, $l = d/2$, where $d = 1.015$ μm. The input light used in these analyses is as the one described in Sec. 4. Adopted materials are as in Sec. 2.

The radiation pattern, assuming free space outside the SiO_2 volume, of the linear OLWA in Fig. 10, is obtained through an HFSS simulation and shown in Fig. 11. It has been compared with the HFSS result obtained for the 2D OLWA in Fig. 1. The result in Fig. 11 shows that the radiation pattern carried out for the 2D OLWA is also representative for the description of directive radiation in the *xy* plane, for the 3D case. However, some small difference is noticeable, and that is due to the different total length of the radiating section $L = Nd$, where N is the number of the perturbation, chosen equal to 60 in the 2D model and equal to 35 in the 3D model to limit the computational requirements.

7. Conclusion

In this work, a highly directive OLWA based on SOI waveguide (made of a Si_3N_4 waveguide comprising a planar periodic structure of silicon strips) has been proposed, whose working principle has been explained by using leaky wave and antenna array factor theory. A two dimensional (2D) implementation has been analyzed in details, and the radiation pattern has been compared to that of a linear OLWA in a 3D space. The highly directive radiation has been designed to be around the bottom transverse direction with 17.5 dB directivity and a 3 dB beam-width of $\Delta\phi_{3\text{dB}} \approx 1.05°$ in SiO_2 environment and with 15.7 dB directivity and a 3 dB beam-width of $\Delta\phi_{3\text{dB}} \approx 1.4°$ in free space environment, when leaky wave phase and attenuation constants were $\beta_{-1} = -2.46 \times 10^5\ \text{m}^{-1}$, and $\alpha = 4.52 \times 10^4\ \text{m}^{-1}$, as extracted by full-wave simulations. Far-field radiation pattern, beam angle and beam-width have been all parameterized in simple terms, based on the complex LW wavenumber $\beta_{-1} + i\alpha$ in the main Brillouin zone. Results have shown that the theoretical predictions agree well with both COMSOL and HFSS full-wave results. For the sake of further investigation, we have observed the relationship of excess index change and attenuation constant with various carrier injection densities in the Si perturbations. Results showed that up to –0.75 dB variation was achievable in the electric far-field radiation magnitude in presence of carrier injection of $10^{19}\ \text{cm}^{-3}$ with respect to the one in absence of carrier injection, at $\phi_{\max}$, with $\beta_{-1} \approx -0.06k_0$, $\alpha = 0.001k_0$ when the perturbation length is 58.2 μm. Based on this investigation, the wave beaming of the optical radiator at a fixed direction could be varied by combining the electronic and optical control to the intrinsic quality factor of the SOI device. Based on reciprocity, the interesting radiation performance exactly holds also for the receiving case, showing very narrow angular selectivity. Our results made the high speed modulation and integration more feasible and promising.

Acknowledgments

This work is supported by National Science Foundation (NSF) Award # ECCS-1028727. The authors also thank Ansys and COMSOL Multiphysics for providing them their simulation tools (HFSS and COMSOL) that were instrumental in this analysis.

#141139 - $15.00 USD Received 14 Jan 2011; revised 8 Mar 2011; accepted 11 Apr 2011; published 20 Apr 2011